CHEMISTRY OF MATERIALS

pubs.acs.org/cm

Article

Size-Dependent Thermodynamic Stability of Copper Sulfide Nanoparticles

Meimin Hu, Jinjia Liu,* Wenping Guo, Xiaotong Liu, Gian-Marco Rignanese,* and Tao Yang*

Cite This: *Chem. Mater.* 2024, 36, 7108−7116

Read Online

ACCESS | Metrics & More | Article Recommendations | Supporting Information

ABSTRACT: Copper sulfide nanoparticles are extensively employed in the field of functional materials. However, synthesizing the desired nanoparticles in a controlled manner is challenging due to the variety of copper sulfide phases and their potential transformations. Here, we utilize a unified theoretical approach combining a high-throughput computational workflow, ab initio atomistic thermodynamics, and the Wulff theorem to study the thermodynamic stability of copper sulfide nanoparticles. Theoretical size-dependent phase diagrams are constructed for the first time, considering various sulfur chemical potentials. This study unveils the evolution of crystal morphology under varying external conditions and underlines the crucial role of surface energy in maintaining the stability of copper sulfide nanoparticles. Our findings offer a theoretical guide for experimental endeavors aimed at synthesizing the desired surface morphology and phases of copper sulfide nanomaterials.

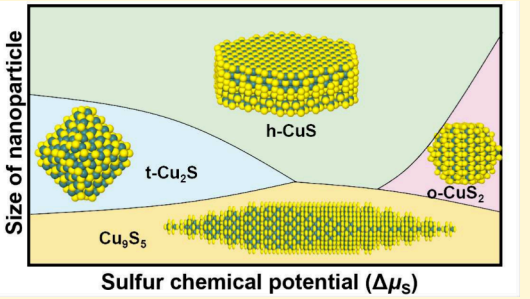

1. INTRODUCTION

Due to their exceptional physical properties, copper sulfides (Cu_xS_y) constitute an important class of functional materials widely used in photocatalysis, solar cells, thermoelectric materials, and resistive switching devices.[1−4] Serving as nanomaterials, their performance is closely associated with factors such as the chemical composition, crystal phase, morphology, and particle size, among others. Therefore, uncovering the structure−property relationship, followed by meticulous design and synthesis of the intended structure, is a crucial prerequisite for achieving materials with exceptional performance.

Because of the high mobility of copper within the sulfur sublattice, there are numerous copper sulfide phases which can easily undergo switchable transformation even under ambient conditions.[5] To date, various Cu_xS_y from copper-rich to sulfur-rich phases have been observed in experiments,[6−8] and their transformations have been extensively investigated experimentally. For copper-rich phases, Cu_2S is known to exhibit a monoclinic phase (low chalcocite) at temperatures below 104 °C. It undergoes a transformation to a hexagonal phase (high chalcocite) between 104 and 436 °C, and it further transitions into a cubic phase (cubic chalcocite) above 436 °C.[9−12] It has also been proven that the hexagonal covellite *CuS* with space group *P*63/*mmc* is thermodynamically stable at room temperature. However, below 55 K, a transformation to an orthorhombic structure (*CuS*-*Cmcm*) occurs.[13−15] Between 278 and 354 °C, covellite can decompose into Cu_7S_4, which ultimately converts into Cu_2S above 500 °C.[16] For sulfur-rich phases, villamaninite (CuS_2) can be preserved at room temperature and ambient pressure, even though it is synthesized under high temperature and pressure conditions. In the presence of air, it tends to decompose into covellite (*CuS*) between 200 and 300 °C and into chalcocite (Cu_2S) and sulfur when the temperature increases to 400−475 °C.[17,18]

Although many experimental studies have been conducted, a complete understanding of the phase transition patterns of copper sulfide nanomaterials has not yet been established. Indeed, for Cu_xS_y nanoparticles, the stability and phase transformations also depend on their morphology and size[19,20] due to the substantial contribution of the surface energy to their total free energy. To achieve the controllable synthesis of single crystals with the desired surface morphology, it is therefore essential to clarify the impact of morphology and size on the nanoparticle stability. However, synthesized nanoparticles are typically polycrystalline, and their surface structures and morphologies are highly sensitive to their surroundings. State-of-the-art methods, such as environmental transmission electron microscopy (ETEM), are unable to capture the evolution of the surface structure and morphology under varying external conditions.[21−23] Besides, measuring the surface energy is also a significant challenge by experimental methods. Therefore, the experimental measure-

Received: March 19, 2024
Revised: July 16, 2024
Accepted: July 16, 2024
Published: July 30, 2024

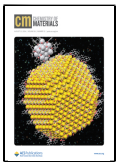

https://doi.org/10.1021/acs.chemmater.4c00817
Chem. Mater. 2024, 36, 7108−7116

ments are statistical in nature, capturing solely aggregated information.

In this framework, condition-free theoretical calculations, specifically density functional theory (DFT) combined with the Wulff theorem, have become an important complement for experiments. They have been widely utilized to discern the evolution of surface structure and morphology under experimental conditions.[24,25] In contrast with experiments, theoretical calculations provide more intrinsic information about the structures and properties of materials. In this work, we use a high-throughput DFT calculation workflow, ab initio atomistic thermodynamics, and Wulff construction to investigate the evolution of surface morphology under various conditions and the effect of size on the thermodynamic stability of copper sulfide nanoparticles. This work provides a universal theoretical pattern for investigating the thermodynamic stability of the nanomaterials.

2. COMPUTATIONAL DETAILS

2.1. Methods. The calculation workflow is presented in Figure 1. All DFT calculations were performed using the

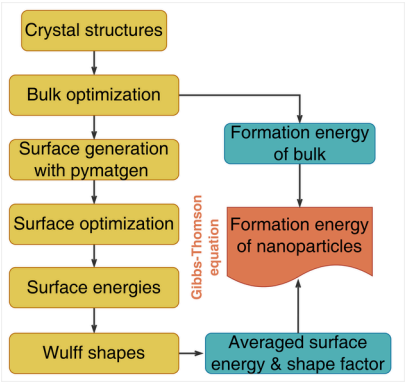

Figure 1. Workflow for formation energy calculation of nanoparticles.

Vienna Ab initio Simulation Package (VASP).[26,27] The interaction between the ion nuclei and the electrons was described using the projector augmented wave (PAW) potential.[28] The exchange-correlation energy was approximated using the regularized-restored strongly constrained and appropriately normed (r^2SCAN)[29] functional within the meta-GGA framework. This functional typically predicts more accurate thermodynamic properties compared to SCAN and PBEsol for solid materials.[30] A plane wave cutoff energy of 450 eV was chosen for the calculations. During the optimization of the bulk phase, both the lattice parameters and atomic positions were allowed to relax. For the surface energy calculations, the lattice parameters were kept fixed at their bulk values, allowing only for the atomic positions to relax. For all of these relaxations, the tolerance on the forces acting on the system was used as the convergence criterion, setting a threshold of 0.03 eV/Å. For the electron self-consistent iterations, the energy convergence criterion was set to 10^{-5} eV. For the sampling of the Brillouin zone, *k*-point grids were generated automatically using a KSPACING value of 0.3 $Å^{-1}$.

2.2. Models. In this work, we focused on eight experimental observed copper sulfides going from copper-rich to sulfur-rich phases, namely, two Cu_2S (*c*- and *t*-), one Cu_7S_4, one Cu_9S_5, two *CuS* (*o*- and *h*-), and two CuS_2 (*c*- and *o*-) phases. The different polymorphs are distinguished using a prefix letter indicating the lattice symmetry: *c* for cubic, *t* for tetragonal, *h* for hexagonal, and *o* for orthorhombic. Their atomistic crystal structures are reported in Figure 2, as

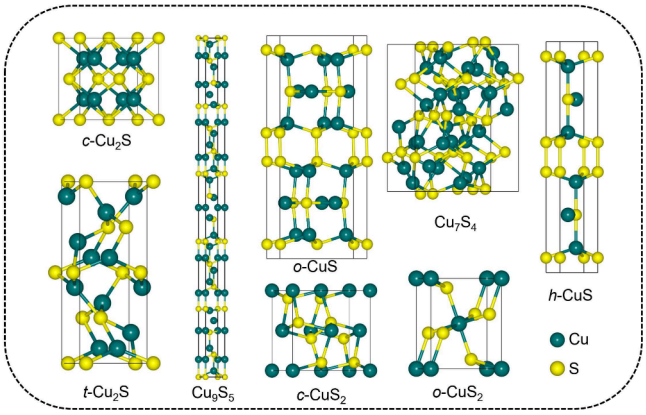

Figure 2. Crystal structures of the eight different copper sulfide phases. The prefixes *c*, *t*, *h*, and *o* indicate cubic, tetragonal, hexagonal, and orthorhombic polymorphs, respectively.

visualized with the VESTA software.[31] For surface energy calculations, slab models were generated for all the possible orientations up to a maximum Miller index of 2 using pymatgen,[32] and all the possible terminations were taken into account. To eliminate the effect of surface polarization on the surface energy, (1 × 1) slabs with inversion symmetry were chosen with a thickness of at least 15 Å. Very large slab models with more than 200 atoms, particularly for higher Miller index facets, had to be discarded due to the huge computational cost. A vacuum separation of 15 Å was used to eliminate the interactions between periodical slabs in the direction perpendicular to the surface. The detailed information for surface models is provided in Table S1.

3. RESULTS AND DISCUSSION

3.1. Crystal Structure of Copper Sulfides Predicted with r^2SCAN. The calculated lattice parameters (and the corresponding volumes) are reported in Table 1 for the eight selected phases. The crystal structures of Cu_2S are somewhat complicated. Its tetragonal polymorph (t-Cu_2S) can be seen as a variation of monoclinic α-chalcocite with reduced symmetry. The structure of this tetragonal phase was elucidated and documented by Janosi,[33] revealing a $P4_32_12$ space group with lattice parameters $a = b = 3.996$ Å and $c = 11.287$ Å. The corresponding calculated values with r^2SCAN are $a = b = 4.059$ Å and $c = 10.590$ Å. The lattice constant in the *c* direction is underestimated with a relative error (RE) of 6.2% (which is more important than in typical DFT calculations). Cu_2S also shows a cubic (anti)fluorite structure with a space group of Fm-$3m$ for temperatures above 743 K. The lattice constant has been measured to be $a = b = c = 5.735$ Å,[10] while our calculated value is 5.553 Å (hence showing a RE of 3.2%). In experimental conditions, defect formation in Cu_2S crystals inevitably leads to the formation of $Cu_{2-x}S$ phases. Two representative phases are $Cu_{1.8}S$ (also known as Cu_9S_5) and $Cu_{1.75}S$ (also known as Cu_7S_4). Digenite (Cu_9S_5) presents the R-$3m$ space group and is a metastable phase similar to tetragonal Cu_2S, which can be produced in ambient atmosphere,[34,35] while Cu_7S_4 has an orthorhombic structure and shows the *Pnma* space group, where the copper atoms are

https://doi.org/10.1021/acs.chemmater.4c00817
Chem. Mater. 2024, 36, 7108−7116

Table 1. Calculated Lattice Parameters for the Eight Copper Sulfide Phases

	c-Cu_2S	*t*-Cu_2S	Cu_9S_5	Cu_7S_4	*o*-*CuS*	*h*-*CuS*	*c*-CuS_2	*o*-CuS_2
space group	*Fm*-3*m*	$P4_32_12$	*R*-3*m*	*Pnma*	*Cmcm*	*P*63/*mmc*	*Pa*3	*Pnnm*
a (Å)	5.553	4.059	3.874	7.831	3.759	3.770	5.782	4.697
b (Å)	5.553	4.059	3.874	7.882	6.559	3.770	5.782	5.808
c (Å)	5.553	10.590	48.217	10.782	16.284	16.282	5.782	3.600
vol ($Å^3$/unit)	42.807	43.624	208.873	166.371	33.463	33.389	48.334	49.095

located in the interstitial sites of the face-centered cubic framework, which is approximately formed by the sulfur atoms.[36] The calculated lattice constants are a = 7.831, b = 7.882, and c = 10.782 Å. Compared to the experimental values of a = 7.38 Å, b = 7.89 Å, and c = 10.77 Å,[37] there is a slight overestimation (RE of 6.1%) in the a direction. Compared to Cu_2S, the crystal structure *CuS* is more established with only two reported polymorphs: hexagonal (*h-CuS*) and orthorhombic (*o-CuS*). In the study of Fjellvg et al., powder X-ray and neutron diffraction methods were used to determine that the *h-CuS* phase is more stable at low temperatures. A crystal distortion and phase transformation can occur from *h-CuS* to *o-CuS* at approximately 55 K.[38] The lattice parameters are found to be very similar for both phases of *CuS*. Available experimental data show that for *h-CuS*, $a = b$ = 3.795 Å and c = 16.34 Å, while for *o-CuS*, a = 3.75 Å, b = 6.55 Å (which is 3.782 $\sqrt{3}$), and c = 16.29 Å. The calculated results using r^2*SCAN* are consistent with the experimental values.[39] Pyrite (*c*-) and marcasite (*o*-) CuS_2 share common features in terms of local coordination. In both crystal structures, each copper atom is surrounded by six nearest-neighbor sulfur atoms in a distorted octahedral environment. Additionally, each sulfur atom bonds to one sulfur and three copper atoms. The lattice parameter for *c*-CuS_2 was observed experimentally to be 5.790 Å,[40] while for *o*-CuS_2, the measured values are of a = 4.651 Å, b = 5.793 Å, and c = 3.532 Å.[41] Our calculations (Table 1) show that the r^2*SCAN* functional accurately reproduces the lattice parameters for both CuS_2 phases. Based on the analysis above, r^2*SCAN* underestimates the lattice parameters for two phases of Cu_2S and Cu_7S_4, with a relative error ranging from 3% to 6%. However, for other copper sulfides, this provides reasonable predictions when compared to experimental values.

3.2. Thermodynamic Stability of Bulk Phase. To evaluate the thermodynamic stability of the eight copper sulfide phases, we calculated their formation energy per copper atom (E_{bulk}, eV/Cu) as shown in eqs 1 and 2, where $E_{Cu_xS_y}$ is the total energy of the unit cell of the bulk Cu_xS_y phase calculated by DFT, E_{Cu}^{ref} is the calculated energy per Cu atom in the pure copper crystal (−10.818 eV with r^2*SCAN* functional), and E_S^{ref} is the energy per S atoms in the α-S_8 crystal (−8.033 eV with r^2*SCAN* functional). In reaction conditions, the free energy of sulfur, termed the sulfur chemical potential (μ_S), also varies with the change of ambient temperature and gaseous pressure. As a result, the formation free energy of Cu_xS_y (Ω_{bulk}) can be calculated according to eq 3. The more Ω_{bulk} is negative, the more the formation of Cu_xS_y is thermodynamically favored. The change of sulfur chemical potential ($\Delta\mu_S$) is defined as shown in eq 4. The range of the sulfur chemical potential is defined as $\mu_S^{min} \le \mu_S \le \mu_S^{max}$, where μ_S^{min} is the minimum sulfur chemical potential in the eight Cu_xS_y crystals while μ_S^{max} is the sulfur chemical potential in pure sulfur crystal. This means that if μ_S is lower than μ_S^{min}, then the Cu_xS_y would be decomposed into elementary copper and sulfur. According to this criterion, $\Delta\mu_S$ was selected to be comprised between −0.30 and 0 eV; details are given in Table S2.

$$xCu + yS \rightarrow Cu_xS_y \quad (1)$$

$$E_{bulk} = \frac{1}{x}E_{Cu_xS_y} - E_{Cu}^{ref} - \frac{y}{x}E_S^{ref} \quad (2)$$

$$\Omega_{bulk} = \frac{1}{x}E_{Cu_xS_y} - E_{Cu}^{ref} - \frac{y}{x}\mu_S \quad (3)$$

$$\Delta\mu_S = \mu_S - \mu_S^{ref} \quad (4)$$

The variation of the formation free energy with the sulfur chemical potential was calculated for the eight bulk copper sulfides, as represented in Figure 3. As Ω_{bulk} linearly decreases

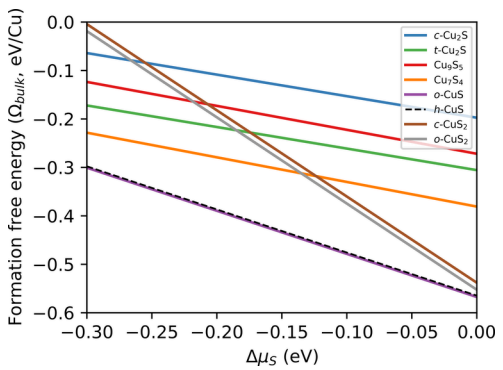

Figure 3. Variation of the formation free energy of bulk copper sulfides (Ω_{bulk}, eV/Cu) with the sulfur chemical potential.

with increasing $\Delta\mu_S$, the formation of copper sulfides becomes more thermodynamically favored at higher sulfur chemical potentials. Furthermore, the slope remains constant for phases with identical stoichiometric ratios. Within the considered range of the sulfur chemical potential, the Ω_{bulk} of the two *CuS* phases (*h-CuS* and *o-CuS*) are nearly identical and lower than that of all the other phases. This indicates that *CuS* is the ground state, in agreement with previous calculations of the convex hull of the *Cu*−*S* system.[42] For two polymorphs of CuS_2, the Ω_{bulk} of the orthorhombic one is always more lower than that of the cubic one during the sulfur chemical potential considered, indicating that the *o*-CuS_2 phase is more stable than *c*-CuS_2. When the $\Delta\mu_S$ < −0.13 eV, the Ω_{bulk} of Cu_7S_4 is lower than that of two CuS_2 phases. However, when $\Delta\mu_S$ is above −0.12 eV, the two CuS_2 atoms (*c*- and *o*-) become more stable than Cu_7S_4. Because the CuS_2 formula has the largest sulfur content, therefore the negative slope of Ω_{bulk} with $\Delta\mu_S$ is larger than that of the other phases. At the critical sulfur chemical potential ($\Delta\mu_S$ = 0 eV), the formation free energy of the *o*-CuS_2 phase is, however, still slightly higher than those of the two *CuS* phases (−0.52 vs −0.56 eV/Cu). The stability of two Cu_2S phases is inferior to that of Cu_7S_4, and the Ω_{bulk} of the tetragonal phase (*t*-Cu_2S) is approximately 0.11 eV/Cu

https://doi.org/10.1021/acs.chemmater.4c00817
Chem. Mater. 2024, 36, 7108−7116

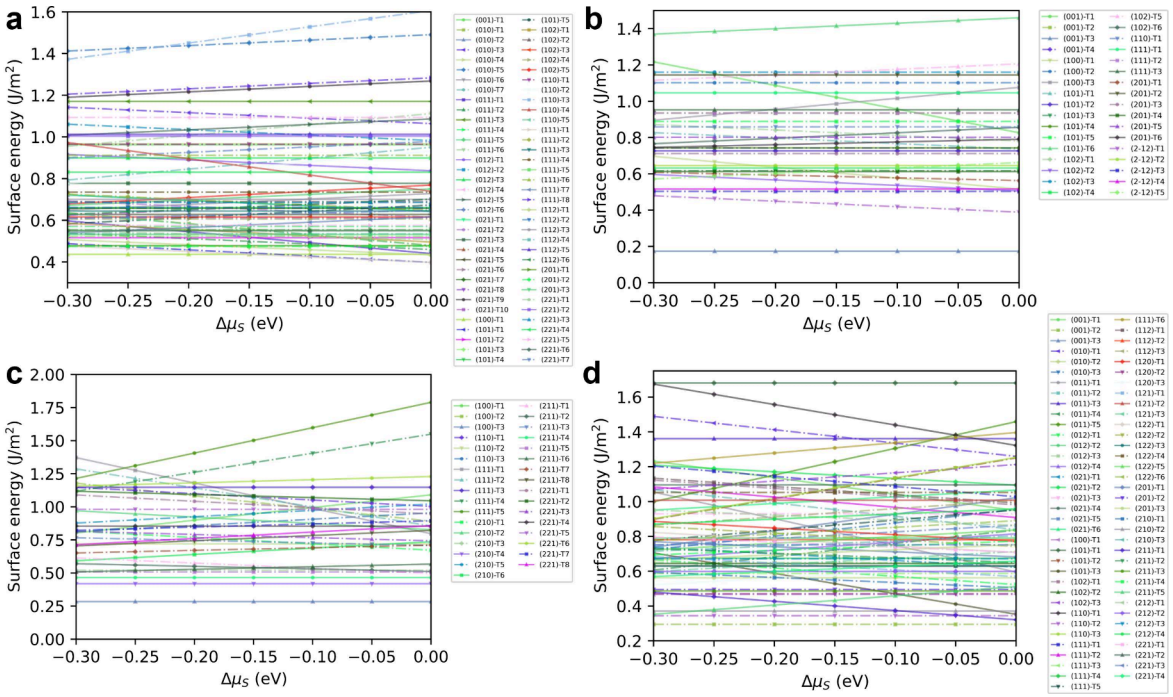

Figure 4. Variation of the calculated surface energy (γ, J/m^2) with the sulfur chemical potential ($\Delta\mu_S$, eV) for (a) *o-CuS*, (b) *h-CuS*, (c) *c-CuS*$_2$, and (d) *o-CuS*$_2$. The coloring scheme for the different orientations and terminations (indicated by the suffix with "T") is reported on the right-hand side of each plot.

lower than that of the cubic Cu_2S phase (*c-Cu*$_2$*S*), while the formation energy of Cu_9S_5 is intermediate between the two Cu_2S phases, which is not as stable as Cu_7S_4.

3.3. Surface Energy and Equilibrium Crystal Morphology. For nanoparticles, the thermodynamic stability is related not only to the composition but also to the morphology and the particle size.[19,20] This is because the contribution of the surface tension cannot be ignored, especially for small particles with a large specific surface area. From a theoretical standpoint, the size-dependent formation free energy of nanoparticles (Ω_{NPs}) can be obtained through an expression similar to the Gibbs−Thomson equation according to eq 5, which was developed by Sun et al.:[43]

$$\Omega_{NPs}(d, \mu_S) = \Omega_{bulk}(\mu_S) + \frac{2}{d}\eta(\mu_S)\rho\overline{\gamma}(\mu_S) \quad (5)$$

In this equation, Ω_{bulk} is the bulk formation free energy calculated with eq 3, d is the diameter of nanoparticles (nm), ρ is the volume normalized per copper atom, η is the dimensionless shape factor (area/volume$^{2/3}$), and $\overline{\gamma}$ is the averaged surface free energy (J/m^2). The values of η and ρ can be obtained through the Wulff construction based on the calculated surface energy. This approximation has been successfully employed to predict the phase transformation of molybdenum and tungsten carbide nanoparticles.[44] To evaluate the thermodynamic stability of copper sulfide nanoparticles, it is necessary to calculate the surface free energy (γ) for different directions and to establish the corresponding Wulff construction. The surface free energy can be calculated using eq 6:

$$\gamma = \frac{1}{2A}\left[E_{slab}(N_{Cu}, N_S) - \frac{N_{Cu}}{x}E_{Cu_xS_y} + \left(\frac{yN_{Cu}}{x} - N_S\right)\mu_S\right] \quad (6)$$

where E_{slab} represents the total energy of the slab models, $E_{Cu_xS_y}$ corresponds to the energy associated with a unit cell of bulk copper sulfide, N_{Cu} and N_S are the number of Cu and S atoms in the slab models, and A is the cross-sectional area of the slab models. In this work, we utilized the automatic workflow provided by Pymatgen to calculate the surface energies and to establish the related Wulff construction. Figure 4 and Figure S1 present the surface energy calculated using eq 6 for the eight copper sulfides for different orientations and terminations. In what follows, we will consider only two *CuS* and two *CuS*$_2$ polymorphs as examples to illustrate the variation of the surface energy with the sulfur chemical potential. The calculation results show that the surface free energy of the sulfur-rich (sulfur-poor) surfaces increases (decreases) gradually with increasing sulfur chemical potential. For surfaces with stoichiometric ratios, the surface free energy remains unaffected by the ambient sulfur chemical potential.

For the *o-CuS* phase, we calculated the surface energy for 13 orientations with all of their possible terminations (i.e., a total of 70 combinations), as reported in Figure 4a. According to these calculations, when the change of the sulfur chemical potential ($\Delta\mu_S$) is lower than −0.15 eV, the (100) surface is the most stable surface with a surface energy of 0.436 J/m^2. Note that this surface has only one possible termination. When $\Delta\mu_S$ is above −0.15 eV, the surface energy of the (111) facet becomes lower than that for other orientations and terminations, though it is close to the surface energy of the (101) orientation. For the *h-CuS* phase (Figure 4b), we calculated the surface energy for 8 orientations with all their possible terminations (i.e., a total of 34 combinations). The most thermodynamically stable surface within the considered sulfur chemical potential range is the (001) surface with a stoichiometric ratio termination. The corresponding calculated surface energy is 0.173 J/m^2. Ángel Morales-García and co-

https://doi.org/10.1021/acs.chemmater.4c00817
Chem. Mater. 2024, 36, 7108−7116

workers also previously calculated the surface energy of *h-CuS* using PBE + *U* (U_{eff} = 5.0 eV). Likewise, they found that the (001) surface is the most stable, with a calculated surface energy of 0.16 J/m^2,[45] which is consistent with our results with *r^{2}SCAN*.

With regard to the pyrite *c-CuS_2* phase (Figure 4c), we calculated the surface energies for 6 orientations with all their possible terminations (i.e., a total of 33 combinations). Our results indicate that the (100) orientation with a stoichiometric ratio termination has the lowest surface energy (0.284 J/m^2), followed by the (210) orientation (0.419 J/m^2). Interestingly, while previous studies have systematically investigated the surface stability of pyrite *FeS_2*[46,47] and *CoS_2*,[48] the surface energy of *c-CuS_2* had not been reported so far. Therefore, this study provides a valuable complement to the surface science of pyrite-type compounds. For the *o-CuS_2* phase (Figure 4d), 19 different orientations with all of their possible terminations (i.e., a total of 71 combinations) were cleaved from the bulk crystal structure and used to calculate the surface energy. For all of the considered sulfur chemical potentials, the (001) orientation with a stoichiometric ratio termination is thermodynamically preferable, with a surface energy of 0.295 J/m^2. When $\Delta\mu_S < -0.05$ eV, the second-lowest surface energy is that of the (110) orientation with a stoichiometric ratio termination. Its surface energy of 0.345 J/m^2 is only slightly higher than that of the (001) surface. However, when $\Delta\mu_S > -0.05$ eV, the (211) orientation becomes more stable than the (110) one. When the critical sulfur chemical potential is reached ($\Delta\mu_S$ = 0 eV), the surface energy of the (211) orientation is as low as 0.32 J/m^2, which is very close to the surface energy of the (001) facet. To the best of our knowledge, this work represents the first systematic study of the surface thermodynamic properties of copper sulfides. It can serve as a valuable reference for future studies on corresponding surface properties.

Utilizing the calculated surface energies and the Wulff theorem, we constructed thermodynamic equilibrium crystal morphologies for the selected eight phases of copper sulfide, as illustrated in Figure 5a. The corresponding percentage contribution of each facet to the total surface area is detailed in Table S3. For *c-Cu_2S* in a high sulfur chemical potential environment, the morphology is an octahedron, and the exposed area entirely consists of (111) facets. This is consistent with TEM images obtained in experiments, as shown in Figure 5b,c.[49] However, when the sulfur chemical potential is decreased, the morphology of the octahedron gets truncated and (100) facets appear. When $\Delta\mu_S$ is decreased to −0.30 eV, the percentages of (111) and (100) facets with respect to the total surface area are 94.7% and 5.3%, respectively. For the *t-Cu_2S* polymorph at low $\Delta\mu_S$, the nanoparticles have an irregular octahedral morphology, their surface being dominated by the (102) and (001) facets, accounting for 96% and 4%, respectively. However, at higher $\Delta\mu_S$, the (001) facets disappear, exhibiting a trend similar to that of *c-Cu_2S*.

The morphology of *Cu_9S_5* and *Cu_7S_4* at thermodynamic equilibrium appears to be biconical (Figure 5d), as observed experimentally.[50] In the case of *Cu_9S_5*, only (21$\bar{2}$) facets are present on the exposed surface when $\Delta\mu_S$ = −0.30 eV. However, when $\Delta\mu_S \geq -0.15$ eV, the (21$\bar{2}$) facets disappear and the entire surface is occupied by (101) facets. The exposed surface of *Cu_7S_4* is dominated by (001), (101), (110), and (112) facets for all of the considered $\Delta\mu_S$. As $\Delta\mu_S$ increases,

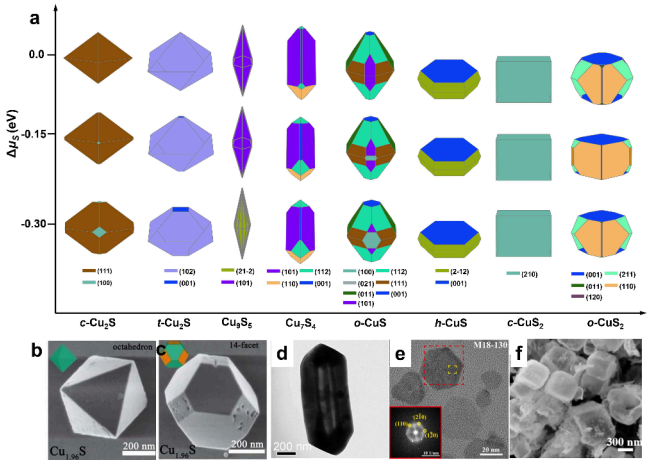

Figure 5. (a) Crystalline morphology evolution of copper sulfides with respect to the sulfur chemical potentials. (b−f) TEM and SEM images for copper sulfides. (b, c) *Cu_2S*. Reproduced with permission from ref 49. Copyright 2012 Royal Society of Chemistry. (d) *$Cu_{2-x}S$*. Reproduced with permission from ref 50. (e) Hexagonal *CuS*. Reproduced with permission from ref 51. Copyright 2021 Wiley. (f) Pyrite *CuS_2*. Reproduced with permission from ref 52. Copyright 2020 Elsevier B.V..

the percentage of (101) facets slightly increases from 70.4% to 78.3%, while that of (112) facets decreases from 13.8% to 1.7%. In contrast, the percentages of (001) and (110) facets are almost unaffected by the sulfur chemical potential.

For *o-CuS* nanoparticles, the (011), (111), and (112) facets dominate, accounting together for 80% of the total surface area. The proportion of (112) facets decreases from 38.9% to 34% as $\Delta\mu_S$ increases from −0.30 to 0 eV, while the proportion of (011) and (111) facets increases with increasing sulfur chemical potential. The (021) and (100) facets only appear at lower sulfur chemical potentials, and their proportions are both below 10%. The detailed information can be found in Table S3. A single crystal of *h-CuS* has been successfully synthesized and characterized using TEM technology.[51] The crystal appears as a 2D plate, as shown in Figure 5e, which is consistent with our predicted morphologies under different sulfur chemical potentials. Our calculations indicate that the surface of *h-CuS* particles is dominated by (001) and (2$\bar{1}$2) facets, with an almost equal exposed percentage. Our calculations show that cubic pyrite *CuS_2* has a morphology resembling a Rubik's cube, with the (210) facets occupying the entire surface (Figure 5a). Interestingly, the shape of *CuS_2* microcrystals obtained by He and co-workers using the sacrificial template method (see the scanning electron microscopy image[52] in Figure 5f) is very similar to our predicted Wulff morphology. The exposed surface of orthorhombic *CuS_2* is dominated by (001), (110), and (211) facets, which together cover over 90% of the total surface area. The contribution of (120) facets is independent of the sulfur chemical potential, and it only occupies 0.9% of the total surface, while the (011), (210), (012), and (101) facets only start to appear at higher sulfur chemical potentials. The corresponding ratios can be found in Table S3.

As is well-known, the chemical potential is associated with the external temperature and gaseous pressure. Therefore, our systematic study of the surface energy and crystal morphology at different sulfur chemical potentials provides a theoretical

https://doi.org/10.1021/acs.chemmater.4c00817
Chem. Mater. 2024, 36, 7108−7116

Table 2. Shape Factor (η), Averaged Surface Energy ($\overline{\gamma}$, J/m^2), and Volume (ρ) of the Different Copper Sulfides Investigated Here at Different Sulfur Chemical Potentials

	shape factor η			averaged surface energy $\overline{\gamma}$ (J/m^2)			volume ρ (Å^3/Cu)
	$\Delta\mu_S$ (eV)			$\Delta\mu_S$ (eV)			–
	−0.30	−0.15	0	−0.30	−0.15	0	–
c-Cu_2S	5.562	5.703	5.719	0.342	0.244	0.153	21.403
t-Cu_2S	5.644	5.715	5.728	0.190	0.104	0.020	21.812
Cu_9S_5	10.357	9.665	9.665	0.021	0.018	0.017	23.208
Cu_7S_4	6.316	6.419	6.884	0.333	0.295	0.212	23.767
o-*CuS*	5.544	5.612	5.693	0.522	0.481	0.430	33.463
h-*CuS*	6.207	6.047	5.891	0.311	0.298	0.283	33.389
c-CuS_2	6.000	6.000	6.000	0.284	0.284	0.284	48.334
o-CuS_2	5.812	5.911	5.775	0.331	0.333	0.323	49.095

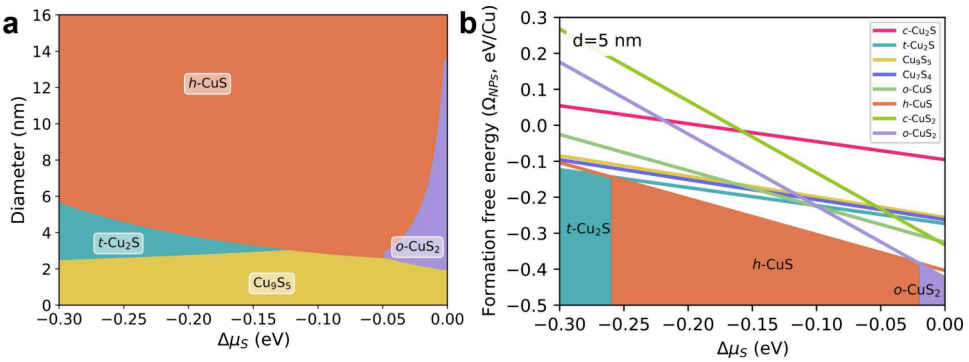

Figure 6. (a) Phase evolution of copper sulfide nanoparticles with the particle size and the sulfur chemical potential. (b) Variation of the formation energy of copper sulfide nanoparticles (Ω_{NPs}, eV/Cu) with the sulfur chemical potential when the diameter of nanoparticles is 5 nm.

guideline for experiments to modulate the crystal morphology by adjusting the synthesis conditions.

3.4. Phase Evolution of Copper Sulfide Nanoparticles. Using the calculated Wulff construction, we can determine the shape factor (η) and average surface energy ($\overline{\gamma}$) at various chemical potentials (Table 2). With these parameters, the size-dependent formation energy of the nanoparticle (Ω_{NPs}) was calculated by using eq 5. Figure 6a shows the phase evolution of copper sulfide nanoparticles at different sulfur chemical potentials and particle sizes. Based on our calculations, the particle size has a significant effect on the thermodynamic stability of Cu_xS_y nanoparticles due to the substantial contribution of the surface energy to the total free energy of the nanoparticles, particularly for small-sized particles with a high area-to-volume ratio.

Figure 6a shows that when the particle diameter is smaller than 2 nm, the formation of Cu_9S_5 is thermodynamically preferable over all of the other phases, even when varying the sulfur chemical potentials. The *t*-Cu_2S phase can be formed under a low sulfur chemical potential ($\Delta\mu_S < -0.13$ eV) when the particle diameter is between 2 and 6 nm. For the sulfur-rich phases, the *o*-CuS_2 phase is thermodynamically preferred at high sulfur chemical potentials ($\Delta\mu_S > -0.05$ eV) for intermediate particle sizes with diameters between 2 and 14 nm. When the particle size is increased, their formation requires higher sulfur chemical potentials. It is worth noting that the *h*-*CuS* phase may appear for a wide range of sizes and of sulfur chemical potentials. This is especially true when the particle diameter is beyond 14 nm, as the formation of *h*-*CuS* is favored over all of the other phases. According to these calculations, we find that the trend of phase evolution for nanoparticle is different from that for bulk phase in Figure 3, which shows that the *o*-*CuS* and *h*-*CuS* is the most stable phases, the reason is that for copper-rich phases, such as Cu_9S_5 and *t*-Cu_2S, the surface energy of their facets is usually lower than that of other phases, especially for *o*-*CuS* and *h*-*CuS*, resulting in the enhanced stability of small-size copper-rich nanoparticles. Various methods have been used to synthesize copper sulfide nanoparticles in experiments. Upon reviewing the literature, it was found that the reported particle size for *h*-*CuS* is typically over 10 nm.[53−56] Sithole reported a one-step synthesis of Cu_9S_5 nanoparticles ranging from 1.0 to 2.6 nm.[57] The size distribution for Cu_2S nanoparticles ranges from 4 to 18 nm.[58,59] The size of the nanoparticles is influenced by many factors in the synthesis process. The Cu_xS_y particles described in all of these experiments are well aligned with our predictions, suggesting that controlling the particle growth is significantly influenced by the thermodynamic formation energy.

Figure 6b shows the variation of the formation free energy of 5 nm diameter Cu_xS_y nanoparticles as a function of the sulfur chemical potential. When $\Delta\mu_S < -0.26$ eV, the *t*-Cu_2S nanoparticles have the lowest Ω_{NPs}. When -0.26 eV $< \Delta\mu_S < -0.02$ eV, the *h*-*CuS* nanoparticles are preferred. Finally, when $\Delta\mu_S > -0.02$ eV, the *o*-CuS_2 nanoparticles have the lowest Ω_{NPs} and can thus be formed. In Figure 3, it was shown that the Ω_{bulk} of *o*-*CuS* and *h*-*CuS* is lower than that of the other phases for all the considered sulfur chemical potentials. This suggests that from bulk phase to nanoparticles the stability can be modulated by the contribution of the surface free energy.

https://doi.org/10.1021/acs.chemmater.4c00817
Chem. Mater. 2024, 36, 7108−7116

4. CONCLUSIONS

In this study, we employed a unified high-throughput DFT computational workflow, coupled with ab initio atomistic thermodynamics and Wulff theory, to investigate the thermodynamic stability of the bulk, surface, and nanoparticles of eight copper sulfides at varying sulfur chemical potentials. For the bulk, the formation energies of two *CuS* phases are similar and much lower than those of all the other compounds. The surface free energy and the crystal morphology vary with the change of the sulfur chemical potential. Considering the contribution of the surface energy to the total free energy of nanoparticles, the phase diagram of Cu_xS_y shows that Cu_9S_5 nanoparticles could be stabilized when the diameter is below 2 nm. The *t*-Cu_2S phase appears at lower sulfur chemical potential when the particle diameter is between 2 and 6 nm. The *o*-CuS_2 phase exists at a higher sulfur chemical potential when the size is moderate. When the particle diameter is >14 nm, the formation of *h-CuS* is thermodynamically more favorable than all other phases.

This study not only provides a clear graphical representation of the evolution of the surface structure and crystal morphology of Cu_xS_y under changing external conditions but also elucidates the pivotal role of the particle size, particularly through the surface energy, in nanoparticle stability. This insight offers valuable guidance for experiments targeting the synthesis of desired phases through the modulation of particle size and experimental conditions.

■ ASSOCIATED CONTENT

Supporting Information

The Supporting Information is available free of charge at https://pubs.acs.org/doi/10.1021/acs.chemmater.4c00817.

Information on surface energy calculations; chemical potential range; exposed surface area; calculated surface energy (PDF)

■ AUTHOR INFORMATION

Corresponding Authors

Jinjia Liu − *State Key Laboratory of Coal Conversion, Institute of Coal Chemistry, Chinese Academy of Sciences, Taiyuan 030001, China; National Energy Center for Coal to Clean Fuels, Synfuels China Co., Ltd., Beijing 101400, China; Institute of Condensed Matter and Nanosciences, Université catholique de Louvain, Louvain-la-Neuve 1348, Belgium;* orcid.org/0000-0002-0795-6561; Email: liujinjia@synfuelschina.com.cn

Gian-Marco Rignanese − *Institute of Condensed Matter and Nanosciences, Université catholique de Louvain, Louvain-la-Neuve 1348, Belgium;* orcid.org/0000-0002-1422-1205; Email: gian-marco.rignanese@uclouvain.be

Tao Yang − *Beijing Advanced Innovation Center for Materials Genome Engineering, Beijing Information Science and Technology University, Beijing 100101, China; School of Computer Science, Beijing Information Science and Technology University, Beijing 100101, China;* Email: ytyangmei@bistu.edu.cn

Authors

Meimin Hu − *State Key Laboratory of Coal Conversion, Institute of Coal Chemistry, Chinese Academy of Sciences, Taiyuan 030001, China; National Energy Center for Coal to Clean Fuels, Synfuels China Co., Ltd., Beijing 101400, China; Inner Mongolia University of Technology, Huhhot 010051, China*

Wenping Guo − *National Energy Center for Coal to Clean Fuels, Synfuels China Co., Ltd., Beijing 101400, China*

Xiaotong Liu − *Institute of Condensed Matter and Nanosciences, Université catholique de Louvain, Louvain-la-Neuve 1348, Belgium; Beijing Advanced Innovation Center for Materials Genome Engineering, Beijing Information Science and Technology University, Beijing 100101, China; School of Computer Science, Beijing Information Science and Technology University, Beijing 100101, China*

Complete contact information is available at: https://pubs.acs.org/10.1021/acs.chemmater.4c00817

Notes

The authors declare no competing financial interest.

■ ACKNOWLEDGMENTS

The authors are grateful for the financial support from the National Natural Science Foundation of China (Nos. 22272009, 22202224) and the funding support from Beijing Advanced Innovation Center for Materials Genome Engineering, Synfuels China, Co. Ltd.

■ REFERENCES

(1) Wang, M.; Xie, F.; Li, W.; Chen, M.; Zhao, Y. Preparation of various kinds of copper sulfides in a facile way and the enhanced catalytic activity by visible light. *J. Mater. Chem. A* **2013**, *1*, 8616−8621.

(2) Yuan, K.; Wu, J.; Liu, M.; Zhang, L.; Xu, F.; Chen, L.; Huang, F. Fabrication and microstructure of p-type transparent conducting CuS thin film and its application in dye-sensitized solar cell. *Appl. Phys. Lett.* **2008**, *93*, 132106.

(3) Tarachand, T.; Hussain, S.; Lalla, N. P.; Kuo, Y.-K.; Lakhani, A.; Sathe, V. G.; Deshpande, U.; Okram, G. S. others Thermoelectric properties of Ag-doped CuS nanocomposites synthesized by a facile polyol method. *Phys. Chem. Chem. Phys.* **2018**, *20*, 5926−5935.

(4) Zhu, Y.-D.; Peng, J.; Jiang, L.-P.; Zhu, J.-J. Fluorescent immunosensor based on CuS nanoparticles for sensitive detection of cancer biomarker. *Analyst* **2014**, *139*, 649−655.

(5) Zimmer, D.; Ruiz-Fuertes, J.; Bayarjargal, L.; Haussühl, E.; Winkler, B.; Zhang, J.; Jin, C.; Milman, V.; Alig, E.; Fink, L. Phase transition of tetragonal copper sulfide Cu_2S at low temperatures. *Phys. Rev. B* **2017**, *96*, 054108.

(6) Zimmer, D.; Ruiz-Fuertes, J.; Bayarjargal, L.; Haussühl, E.; Winkler, B.; Zhang, J.; Jin, C.; Milman, V.; Alig, E.; Fink, L. Phase transition of tetragonal copper sulfide CuS at low temperatures. *Phys. Rev. B* **2017**, *96*, 054108.

(7) Dunn, J.; Muzenda, C. Thermal oxidation of covellite (CuS). *Thermochim. Acta* **2001**, *369*, 117−123.

(8) Xie, Y.; Riedinger, A.; Prato, M.; Casu, A.; Genovese, A.; Guardia, P.; Sottini, S.; Sangregorio, C.; Miszta, K.; Ghosh, S.; Pellegrino, T.; Manna, L. Copper sulfide nanocrystals with tunable composition by reduction of covellite nanocrystals with Cu+ ions. *J. Am. Chem. Soc.* **2013**, *135*, 17630−17637.

(9) Xu, Q.; Huang, B.; Zhao, Y.; Yan, Y.; Noufi, R.; Wei, S.-H. Crystal and electronic structures of Cu_xS solar cell absorbers. *Appl. Phys. Lett.* **2012**, *100*, 061906.

(10) Buerger, M.; Wuensch, B. J. Distribution of atoms in high chalcocite, Cu_2S. *Science* **1963**, *141*, 276−277.

(11) Will, G.; Hinze, E.; Abdelrahman, A. R. M. Crystal structure analysis and refinement of digenite, $Cu_{1.8}S$, in the temperature range 20 to 500 °C under controlled sulfur partial pressure. *Eur. J. Mineral.* **2002**, *14*, 591−598.

(12) Buerger, M.; Wuensch, B. The crystal structure of chalcocite, Cu_2S. *Mineral. Soc. Am., Spec. Pap.* **1963**, *1*, 164−170.

(13) Evans, H.; Konnert, J. Crystal structure refinement of covellite. *Am. Mineral.* **1976**, *61*, 996−1000.
(14) Oftedal, I. Die kristallstruktur des covellins (CuS). *Z. Kristallogr. - Cryst. Mater.* **1932**, *83*, 9−25.
(15) Fjellvåg, H.; Grønvold, F.; Stølen, S.; Andresen, A. F.; Müller-Käfer, R.; Simon, A. Low-temperature structural distortion in CuS. *Z. Kristallogr.* **1988**, *184*, 111−121.
(16) Brunetti, B.; Piacente, V.; Scardala, P. Study on sulfur vaporization from covellite (CuS) and anilite ($Cu_{1.75}S$). *J. Alloys Compd.* **1994**, *206*, 113−119.
(17) Nicpon, P.; Meek, D. W. A Novel Synthesis of Arylphosphine Selenides. Reaction of Arylphosphines with Potassium Selenocyanate. *Inorg. Chem.* **1966**, *5*, 1297−1298.
(18) Bither, T.; Prewitt, C.; Gillson, J.; Bierstedt, P.; Flippen, R.; Young, H. New transition metal dichalcogenides formed at high pressure. *Solid State Commun.* **1966**, *4*, 533−535.
(19) Navrotsky, A.; Mazeina, L.; Majzlan, J. Size-driven structural and thermodynamic complexity in iron oxides. *Science* **2008**, *319*, 1635−1638.
(20) Navrotsky, A.; Ma, C.; Lilova, K.; Birkner, N. Nanophase transition metal oxides show large thermodynamically driven shifts in oxidation-reduction equilibria. *Science* **2010**, *330*, 199−201.
(21) Hwang, S.; Chen, X.; Zhou, G.; Su, D. In situ transmission electron microscopy on energy-related catalysis. *Adv. Energy Mater.* **2020**, *10*, 1902105.
(22) He, B.; Zhang, Y.; Liu, X.; Chen, L. In-situ transmission electron microscope techniques for heterogeneous catalysis. *ChemCatChem* **2020**, *12*, 1853−1872.
(23) Zhao, X.; Sun, S.; Yang, F.; Li, Y. Atomic-scale evidence of catalyst evolution for the structure-controlled growth of single-walled carbon nanotubes. *Acc. Chem. Res.* **2022**, *55*, 3334−3344.
(24) Boukouvala, C.; Daniel, J.; Ringe, E. Approaches to modelling the shape of nanocrystals. *Nano Convergence* **2021**, *8*, 1−15.
(25) Seif, M. N.; Beck, M. J. Surface excess free energies and equilibrium Wulff shapes in variable chemical environments at finite temperatures. *Appl. Surf. Sci.* **2021**, *540*, 148383.
(26) Kresse, G.; Furthmüller, J. Efficiency of ab-initio total energy calculations for metals and semiconductors using a plane-wave basis set. *Comput. Mater. Sci.* **1996**, *6*, 15−50.
(27) Kresse, G.; Furthmüller, J. Efficient iterative schemes for ab initio total-energy calculations using a plane-wave basis set. *Phys. Rev. B* **1996**, *54*, 11169.
(28) Blöchl, P. E. Projector augmented-wave method. *Phys. Rev. B* **1994**, *50*, 17953.
(29) Furness, J. W.; Kaplan, A. D.; Ning, J.; Perdew, J. P.; Sun, J. Accurate and numerically efficient r^2SCAN meta-generalized gradient approximation. *J. Phys. Chem. Lett.* **2020**, *11*, 8208−8215.
(30) Kingsbury, R.; Gupta, A. S.; Bartel, C. J.; Munro, J. M.; Dwaraknath, S.; Horton, M.; Persson, K. A. Performance comparison of r^2SCAN and SCAN metaGGA density functionals for solid materials via an automated, high-throughput computational workflow. *Phys. Rev. Mater.* **2022**, *6*, 013801.
(31) Momma, K.; Izumi, F. VESTA3 for three-dimensional visualization of crystal, volumetric and morphology data. *J. Appl. Crystallogr.* **2011**, *44*, 1272−1276.
(32) Ong, S. P.; Richards, W. D.; Jain, A.; Hautier, G.; Kocher, M.; Cholia, S.; Gunter, D.; Chevrier, V. L.; Persson, K. A.; Ceder, G. Python Materials Genomics (pymatgen): A robust, open-source python library for materials analysis. *Comput. Mater. Sci.* **2013**, *68*, 314−319.
(33) Janosi, A. La structure du sulfure cuivreux quadratique. *Acta Crystallogr.* **1964**, *17*, 311−312.
(34) Skinner, B. J. Stability of the tetragonal polymorph of Cu_2S. *Econ. Geol.* **1970**, *65*, 724−728.
(35) Liu, L.; Zhong, H.; Bai, Z.; Zhang, T.; Fu, W.; Shi, L.; Xie, H.; Deng, L.; Zou, B. Controllable transformation from rhombohedral $Cu_{1.8}S$ nanocrystals to hexagonal CuS clusters: phase-and composition-dependent plasmonic properties. *Chem. Mater.* **2013**, *25*, 4828−4834.
(36) Morimoto, N.; Koto, K. Phase relations of the Cu-S system at low temperatures: stability of anilite. *Am. Mineral.* **1970**, *55*, 106−117.
(37) Beere, H. K.; Pakhira, S.; Yadav, P.; Singh, A.; Upadhyay, S. N.; Naik, P. B.; Kotrappanavar, N. S.; Ghosh, D. Realizing Favorable Synergism Toward Efficient Hydrogen Evolution Reaction with Heterojunction Engineered $Cu_7S_4/CuS_2/NiS_2$ and Functionalized Carbon Sheet Heterostructures. *Adv. Mater. Interfaces* **2022**, *9*, 2201478.
(38) Fjellvåg, H.; Grønvold, F.; Stølen, S.; Andresen, A. F.; Müller-Käfer, R.; Simon, A. Low-temperature structural distortion in CuS. *Z. Kristallogr.* **1988**, *184*, 111−121.
(39) Chaki, S. H.; Tailor, J.; Deshpande, M. Covellite CuS-Single crystal growth by chemical vapour transport (CVT) technique and characterization. *Mater. Sci. Semicond. Process.* **2014**, *27*, 577−585.
(40) Bither, T. A.; Bouchard, R.; Cloud, W.; Donohue, P.; Siemons, W. Transition metal pyrite dichalcogenides. High-pressure synthesis and correlation of properties. *Inorg. Chem.* **1968**, *7*, 2208−2220.
(41) Kjekshus, A.; Rakke, T. Preparations and properties of magnesium, copper, zinc and cadmium dichalcogenides. *Acta Chem. Scand.* **1979**, *302*, 080617−04502.
(42) Dennler, G.; Chmielowski, R.; Jacob, S.; Capet, F.; Roussel, P.; Zastrow, S.; Nielsch, K.; Opahle, I.; Madsen, G. K. Are binary copper sulfides/selenides really new and promising thermoelectric materials? *Adv. Energy Mater.* **2014**, *4*, 1301581.
(43) Sun, W.; Kitchaev, D. A.; Kramer, D.; Ceder, G. Non-equilibrium crystallization pathways of manganese oxides in aqueous solution. *Nat. Commun.* **2019**, *10*, 573.
(44) Shrestha, A.; Gao, X.; Hicks, J. C.; Paolucci, C. Nanoparticle size effects on phase stability for molybdenum and tungsten carbides. *Chem. Mater.* **2021**, *33*, 4606−4620.
(45) Morales-García, Á.; He, J.; Soares, A. L.; Duarte, H. A. Surfaces and morphologies of covellite (CuS) nanoparticles by means of ab initio atomistic thermodynamics. *CrystEngComm* **2017**, *19*, 3078−3084.
(46) Xian, H.; Wu, X.; Zhu, J.; Du, R.; Wei, J.; Zhu, R.; He, H. Environmental-sulfur-controlled surface properties of pyrite: a first principles PBE + U study. *Phys. Chem. Miner.* **2021**, *48*, 1−11.
(47) Yang, T.; He, Y.; Liu, X.; Liu, X.; Peng, Q.; Li, N.; Liu, J. Mapping surface morphology and phase evolution of iron sulfide nanoparticles. *CrystEngComm* **2021**, *23*, 5645−5654.
(48) Zhu, Y.-l.; Wang, C.-J.; Gao, F.; Xiao, Z.-x.; Zhao, P.-l.; Wang, J.-y. Calculation on surface energy and electronic properties of CoS_2. *R. Soc. Open Sci.* **2020**, *7*, 191653.
(49) Xu, M.; Wu, H.; Da, P.; Zhao, D.; Zheng, G. Unconventional 0-, 1-, and 2-dimensional single-crystalline copper sulfide nanostructures. *Nanoscale* **2012**, *4*, 1794−1799.
(50) Pei, X.; Zhu, Y.; Du, C.; Peng, H.; Wang, Z.; Ma, X.; Hou, J.; Cao, C. Single-Crystal Copper Sulfide Anode with Fast Ion Diffusion for High-Rate Sodium-Ion Batteries. *ACS Appl. Energy Mater.* **2023**, *6*, 8132−8140.
(51) Zheng, Z.; Yu, P.; Cao, H.; Cheng, M.; Zhou, T.; Lee, L. E.; Ulstrup, J.; Zhang, J.; Engelbrekt, C.; Ma, L. Starch capped atomically thin CuS nanocrystals for efficient photothermal therapy. *Small* **2021**, *17*, 2103461.
(52) He, Y.; Zhang, X.; Wang, S.; Meng, J.; Sui, Y.; Wei, F.; Qi, J.; Meng, Q.; Ren, Y.; Zhuang, D. Rubik's cube-like Ni_3S_4/CuS_2 nanocomposite for high-performance supercapacitors. *J. Alloys Compd.* **2020**, *847*, 156312.
(53) Tetyana, P.; Mphuthi, N.; Jijana, A. N.; Moloto, N.; Shumbula, P. M.; Skepu, A.; Vilakazi, L. S.; Sikhwivhilu, L. Synthesis, characterization, and electrochemical evaluation of copper sulfide nanoparticles and their application for non-enzymatic glucose detection in blood samples. *Nanomater* **2023**, *13*, 481.
(54) Ajibade, P. A.; Botha, N. L. Synthesis and structural studies of copper sulfide nanocrystals. *Results Phys.* **2016**, *6*, 581−589.
(55) Ravele, M. P.; Oyewo, O. A.; Onwudiwe, D. C. Controlled synthesis of CuS and Cu_9S_5 and THEIR application in the photocatalytic mineralization of tetracycline. *Catalysts* **2021**, *11*, 899.

https://doi.org/10.1021/acs.chemmater.4c00817
Chem. Mater. 2024, 36, 7108−7116

(56) Ko, S.; Chung, H. Preparation of C60 Fullerene Nanowhisker−CuS Nanoparticle Composites and Photocatalyst for Rhodamine B Degradation under Blue Light Emitting Diode Irradiation. *Eurasian Chem.-Technol. J.* **2023**, *25*, 65−71.
(57) Sithole, R. K.; Machogo, L. F.; Moloto, M. J.; Gqoba, S. S.; Mubiayi, K. P.; Van Wyk, J.; Moloto, N. One-step synthesis of Cu_3N, Cu_2S and Cu_9S_5 and photocatalytic degradation of methyl orange and methylene blue. *J. Photochem. Photobiol., A* **2020**, *397*, 112577.
(58) Zhang, Y.; Li, X.; Xu, W.; Li, S.; Wang, H.; Li, L. S. The size controlled synthesis and self-assembled of monodisperse Cu_2S nanocrystals. *Mater. Lett.* **2012**, *67*, 117−120.
(59) Huang, H.; Li, F.; Wang, H.; Zheng, X. The size controlled synthesis of Cu_2S/P25 hetero junction solar-energy-materials and their applications in photocatalytic degradation of dyes. *RSC Adv.* **2017**, *7*, 50056−50063.

https://doi.org/10.1021/acs.chemmater.4c00817
Chem. Mater. 2024, 36, 7108−7116